e-ISSN: 2149-4584

Erzincan University Journal of Science and Technology

EJSAT 2026, 19 (2) 158-181

Research Article

Performance Comparison of a Yokeless and Segmented Armature Type Axial Flux Induction Motor in Terms of Rotor Bar Number, Material, and Operating Speed

Harun ASLANER[1*], Mehmet AKAR[2]

[1*]Department of Electrical and Electronics Engineering, Graduate School of Natural and Applied Sciences, Tokat Gaziosmanpaşa University, Türkiye

[2]Department of Electrical and Electronics Engineering, Faculty of Engineering and Architecture, Tokat Gaziosmanpaşa University, Türkiye

Received: 23/03/2026, **Revised:** 04/06/2026, **Accepted:** 16/07/2026, **Published:** 31/08/2026

Abstract

This study provides a detailed examination of the Yokeless and Segmented Armature type (YASA) Axial Flux Induction Motor (AFIM) structure, which is scarcely addressed in the literature. In the study, a YASA-type AFIM with a double-rotor architecture was analysed using Finite Element Analysis (FEA) for five different rotor bar numbers and three operating speeds, while keeping the stator structure constant and employing both aluminium and copper rotor bar materials. The main objective of the study is to systematically compare the effects of rotor bar number, rotor bar material, and operating speed on motor performance, and to provide guidance for future studies. The motor, featuring 6 poles and 9 stator slots, was tested for 29, 31, 35, 37, and 41 rotor bars using both aluminium and copper as rotor bar materials. Analyses at operating speeds of 1000, 2000, and 3000 rpm compared torque, torque ripple, efficiency, and losses. To enable the interpretation of multi-criteria optimization, an Optimal motor configuration for this study was determined using a Normalized Performance Index (NPI). The results indicate that, when copper is used as the rotor bar material, the 41-bar configuration is the most suitable choice across all three operating speeds. When aluminium is used, the 29-bar configuration is optimal at 1000 rpm, whereas the 41-bar configuration is optimal at 2000 and 3000 rpm. The obtained data provide a foundation for needs-based parameter optimization in future YASA-type AFIM designs, facilitating further research in this field.

Keywords – Yokeless and Segmented, Axial Flux Induction Motor, Finite Elements Analysis

Boyunduruksuz ve Segmentli Armatür tipi Eksenel Akılı Asenkron Motorun, Rotor Bar Sayısı, Malzemesi ve Çalışma Hızı Kapsamında Performans Karşılaştırması

Öz

Bu çalışma literatürde oldukça sınırlı sayıda yer bulan Boyunduruksuz ve Segmentli Armatür tipi (YASA) Eksenel Akılı Asenkron Motor (EAASM) yapısını detaylıca ele almaktadır. Çalışmada, YASA tipi çift rotor mimarisine sahip EAASM, stator yapısı sabit tutularak; alüminyum ve bakır rotor bar malzemesi kullanılarak 5 farklı rotor bar sayısı için 3 farklı çalışma hızında Sonlu Eleman Yöntemleri (SEY) ile analiz edilmiştir. Çalışmanın temel amacı; rotor bar sayısı, rotor bar malzemesi ve çalışma hızı parametrelerinin motor performansı üzerindeki etkilerini sistematik olarak kıyaslamak ve bundan sonra yapılacak çalışmalara da kolaylık sağlamaktır. 6 kutup, 9 stator oluğuna sahip motor 29,31,35,37 ve 41 rotor bar sayısı için hem alüminyum hem de bakır rotor bar malzemesi kullanılarak sınanmıştır. 1000,2000 ve 3000 rpm çalışma hızlarının ele alındığı analizlerde tork, tork dalgalanması, verimlilik ve kayıplar kıyaslanmış olup çok kriterli optimizasyonun yorumlanabilmesi adına Normalize Performans İndeksi (NPİ) ile söz konusu çalışma için optimal motor yapısı belirlenmiştir. Analiz sonuçları rotor bar malzemesi olarak bakır kullanılması durumunda 41 bar yapısının 3 farklı çalışma hızında da en uygun seçim olduğunu, alüminyum kullanılması durumunda ise 1000 rpm için 29 bar yapısının, 2000 ve 3000 rpm hızlarında ise 41 bar konfigürasyonunun optimum rotor oluk sayısı olduğunu göstermektedir. Elde edilen veriler, YASA tipi EAASM tasarımı için yapılacak olan ileriki çalışmalar adına ihtiyaç odaklı parametre optimizasyonuna olanak sağlarken, bu kapsamda araştırmacılara kolaylık sağlayacağı öngörülmektedir.

Corresponding Author: h.aslaner06@gmail.com
Cite this Article: Erzincan University Journal of Science and Technology 2026, 19(2)158-181. https://doi.org/10.18185/erzifbed.1914062

Anahtar Kelimeler – Boyunduruksuz ve Segmentli, Eksenel Akılı Asenkron Motor, Sonlu Elemanlar Analizi

1. Introduction

Electric motors have become an indispensable component from the time of their invention to the present day, owing to the convenience they provide. As one of the most important types of loads in both industry and daily life, electric motors account for approximately one-third of the total electrical energy consumption [1,2]. Due to their advantageous cost, low maintenance requirements, and robust performance despite their simple construction, induction motors are among the most widely used types within the family of electric motors. The axial flux motor (AFM), regarded as the first electric generator in history, was invented by Faraday in 1831 as a primitive disk-type machine [3]. However, due to the technological limitations of the period, manufacturing difficulties, and the problems caused by the strong magnetic attraction forces between the stator and rotor, its production remained limited [4]. In recent years, with improvements in manufacturing conditions and the increasing demand for compact designs in terms of volume, AFMs have gained significant popularity and have become a major focus of interest for researchers.

Comparative studies in the literature between conventional radial flux architectures and axial flux structures indicate that AFMs can provide superior performance in terms of efficiency, power density, and power to weight ratio [5,6]. Although AFM structures have predominantly been studied for permanent magnet machines in previous works, the mandatory use of rare-earth elements and the rapidly increasing global energy demand raise concerns for manufacturers regarding magnet-based designs. This situation has led to a growing interest in AFIMs, which do not require permanent magnets. Compared to their radial flux counterparts, AFMs can exhibit better ventilation and cooling performance due to their larger diameter-to-length ratio and the fact that their inner diameter is greater than the shaft diameter [7]. Despite these advantages, the AFM architecture is more complex than radial structures. In this context, AFMs should be addressed using a three-dimensional (3D) approach [8]. During the design stage, the 3D modelling approach requires long analysis times and leads to an increased computational burden [9]. This issue, which results in a loss of time and energy for designers, can be mitigated by employing two-dimensional (2D) linear architectures that enable modelling based on the average diameter of AFMs [10].

The AFIM structure encompasses various topologies that enable its applicability across different applications. These topologies are fundamentally classified into three types: single-sided machines, double-sided machines, and multi-stage machines [11]. The configuration consisting of a single rotor and a single stator is a simple architecture and is preferred for low-power applications [12]. However, it presents certain drawbacks, such as strong magnetic attraction forces between the stator and rotor, deformation of the rotor disk, manufacturing difficulties, and concerns related to bearing wear [13]. Double-sided architectures, which can be realized as double-stator single-rotor or double-rotor single-stator configurations, are among the most commonly used topologies in practical applications. The double-rotor design employed in this study includes two sub-topologies, North–North (NN) and North–South (NS). The primary difference between these two sub-topologies lies in their flux paths. The axial forces supported by the bearings, along with the mechanical components ensuring the connection between the disk and the shaft, and the structural rigidity of the disks, impose limitations on increasing the motor diameter to achieve higher torque [14]. To overcome this limitation, multiple rotor disks and stators can be combined to form a multi-stage motor structure, while also allowing modification of the length to diameter ratio of AFMs [15].

The YASA topology with a double-rotor structure, addressed in this study, is a novel type of AFM that offers significant advantages in torque density and efficiency compared to alternative AFM configurations [16]. In his study, Woolmer conducted FEA of a YASA-type axial flux permanent magnet synchronous machine (AFPMSM), in which the amount of iron in the stator was reduced by 50%, and reported that it achieved 20% higher torque density and efficiency exceeding 94% compared to other AFMs [16]. Chang et al. performed an optimization study on a YASA-type AFPMSM aimed at improving output power by employing a direct cooling system to evaluate its thermal performance, and reported favourable results [17]. Taran et al. compared a double-rotor architecture with a single-sided AFPMSM for a racing vehicle using FEA, concluding that both topologies exhibit similar performance and that the selection should be based on application specific requirements [18]. Huang et al. proposed an AFIM with a YASA topology in a double-rotor, single-stator configuration as a traction motor for electric vehicles [53]. Taking advantage of the YASA topology's ability to eliminate the stator yoke, they utilized a stator made of grain-oriented silicon steel to reduce weight and improve efficiency. They introduced the fundamental topology of the motor, discussed the design methodology, and compared analytical modelling with FEA for performance evaluation [53].

As can be seen from the literature, studies on AFMs with YASA topology have predominantly focused on permanent magnet structures, whereas there is almost no work on induction machines employing the YASA configuration. Therefore, considering the limited available data in the literature, this study aims to provide researchers with a comprehensive evaluation of the YASA-type application for AFIMs. Although aluminium is widely preferred as a rotor bar material in induction motors due to its cost-effectiveness and durability, copper is also extensively used in performance-oriented applications. Daut et al. conducted FEA on a 0.5 HP induction motor to compare copper and aluminium rotor bar materials, reporting that the use of copper resulted in reduced losses and improved performance [19]. In induction motors, the arrangement of stator and rotor slots plays a critical role in minimizing noise and vibration, as well as suppressing harmonic torque components [20]. Gyftakis and Kappatou investigated the effect of rotor slot count (and thus the number of conductor bars) on motor performance by analysing six different designs while keeping the stator structure constant, and concluded that the rotor slot and bar configuration significantly influences motor performance [21]. It is well known that the number of rotor slots in an induction motor determines the slot harmonics, while the number and material of the inserted rotor bars directly influence the cogging torque periodicity, rotor resonance, spatial MMF harmonic interactions, and torque ripple frequency. While selecting the rotor bar number to minimize these effects, the chosen values of 29, 31, 35, 37, and 41 bars distribute the cogging frequency over a wider range, thereby reducing torque ripple and avoiding the mechanical resonance band. For these reasons, these rotor bar counts have been examined in detail in this study.

The YASA-type AFIM considered in this study has been simulated at three different speeds in order to examine its electromagnetic and loss characteristics over a wide speed range. For low-speed operation, the rotor slot structure enhances the starting torque, whereas at high speeds, increased resistance leads to reduced efficiency [22]. In this study, a 6.4 kW YASA-type AFIM with 6 poles and 9 stator slots was taken as the reference machine, and FEA was employed. In order to achieve an effective evaluation, the stator side was kept constant, while designs with 29, 31, 35, 37, and 41 rotor bars (and corresponding slots) were modelled in 2D for both aluminium and copper rotor bar materials, and analyses were carried out over a wide speed range. It is evident that the YASA topology, which enables high efficiency at low volumes due to its compact structure and the elimination of the stator yoke, has predominantly been investigated for AFPMSM in the literature. However, under today's conditions of rapidly increasing energy demand, its application to AFIMs distinguished by their robust structure and economic feasibility, as they do not require rare-earth permanent magnets, deserves further investigation. The main contributions of this study to the literature are summarized as follows.

- The YASA-type AFIM structure, which has been addressed only in a limited number of studies in the literature, has been investigated.
- Aluminium and copper, the two most commonly used conductor materials in the industry, have been simulated and compared for different rotor bar counts.
- The stator structure was kept constant while the number of rotor bars (and their corresponding slots) was varied to investigate the effect of different stator–to-rotor slot combinations on motor performance.
- The motor was analysed over a wide speed range (1000, 2000, and 3000 rpm) and slip region of 1% to 6% to evaluate the impact of speed and slip on motor performance.
- In addition, considering the limited number of sources in the literature regarding the AFIM architecture with YASA topology, the effects of the above-mentioned operating conditions on torque, torque ripple, efficiency, and losses were examined, and a general performance evaluation was conducted to determine the optimum motor configuration.

There are various studies in the literature on the design and performance of AFIMs; however, most of these studies focus on specific design parameters or limited operating conditions. Importantly, the YASA topology addressed in this paper has not been previously studied within the AFIM framework, and existing studies on other AFIM topologies do not provide a comprehensive performance evaluation covering rotor bar count, rotor bar material, and a wide operating speed range. Therefore, a comparison between selected AFIM studies from the literature and the work presented in this paper is provided in Table 1.

Table 1. Comparison of selected AFIM studies from the literature with the present work

Reference	Motor type	Analysis method	Rotor slot/bar configuration analysis	Rotor material analysis	Speed analysis	Main objective
[7]	AFIM-RFIM	2D FEM	None	None	Fixed	Performance comparison between AFIM and RFIM
[8]	AFIM	2D FEM	Rotor slot geometry analysis	Al and Cu	Fixed	Investigation of the effects of rotor slot geometry and squirrel-cage material on AFIM performance

[9]	AFIM	2D FEM	None	None	Fixed	To present an AFIM design optimization for electric vehicles
[35]	AFIM	2D FEM	28-42 bar count	None	Fixed	Upgrading the efficiency class of AFIM to that of an RFIM
[50]	AFIM-AFSRM	3D FEM	Modification of rotor geometry	None	Fixed	Performance comparison between AFIM and AFSRM
[51]	AFIM	3D FEM	None	None	Fixed	Investigation of AFIM's response to variations in the magnetic Circuit
[53]	YASA AFIM	3D FEM	None	None	Fixed	Proposal of a novel AFIM as a traction motor for electric vehicles
This study	YASA AFIM	2D FEM	29-41 bar count	Al and Cu	Variable speeds	Effects of rotor bar count, material, and speed parameters on YASA AFIM

Section 2 provides a detailed examination of the YASA-type AFIM structure. Section 3 describes the methodology for the modelling and analysis of the proposed design. The results and evaluations are presented in Section 4, followed by a general performance assessment in Section 5. Finally, Section 6 concludes the paper by interpreting the results and offering insights and approaches for future research.

YASA-Type AFIM Architecture

In this paper, the YASA topology considered for AFIM was originally designed by Woolmer for the LIFEcar project, and its advantages were presented through comparisons with existing AFMs [16]. In the literature, three main topologies are generally recognized for AFMs, namely single-sided, double-sided, and multi-layered configurations [23]. The double-rotor topology designed in this study [24] features a toroidal winding with an internal stator architecture and is referred to as the TORUS topology [25]. The double-rotor architecture includes two sub-topologies: North–North (NN) and North–South (NS) [11]. In the NS configuration, which enables the YASA topology, the flux path passes through the stator core, eliminating the need for a stator yoke [11]. Figure 1 illustrates the NN topology (a), the NS topology allowing the removal of the stator yoke (b), the YASA topology (c), and a 3D representation of the double-rotor, single-stator configuration (d).

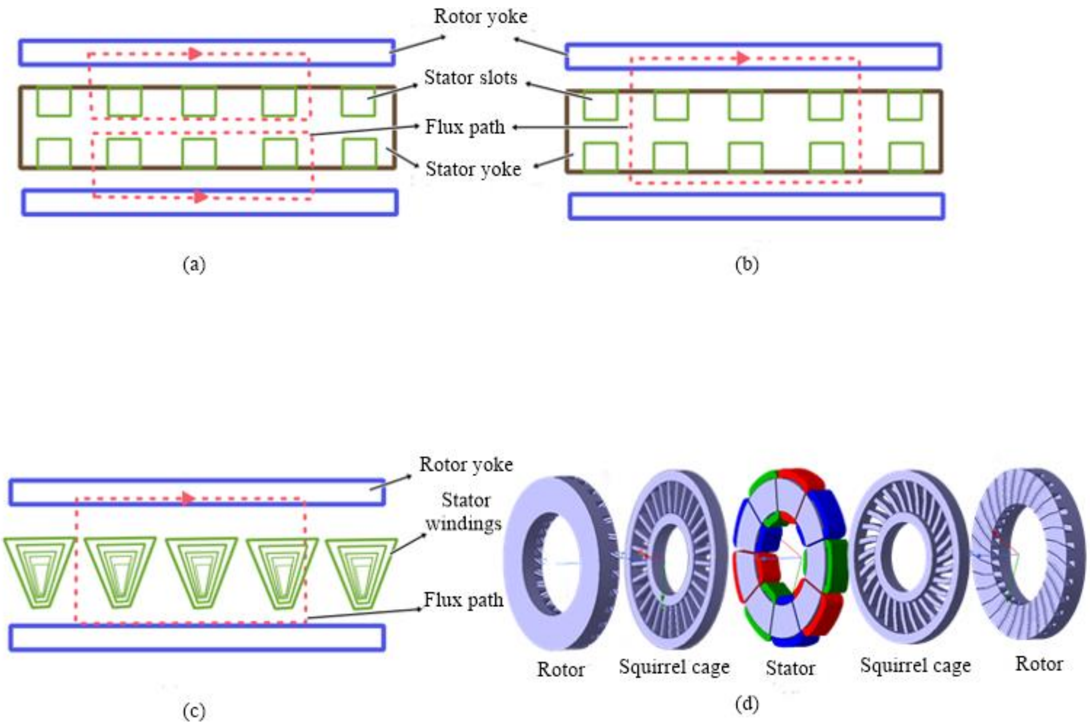

Figure 1. Flux path representation for the NN (a), NS (b), and YASA (c) topologies in the 2D plane, and 3D representation of the double-rotor, single-stator architecture (d).

In order to achieve optimal efficiency from widely used induction motors, it is well recognized that the selection of appropriate materials and the rotor structure is crucial. While it is not possible to select a rotor design that delivers maximum efficiency under all conditions, it is feasible to obtain a rotor configuration tailored to the specific design and application [26]. Aluminium is widely used due to its advantages, such as ease of manufacturing, low cost, and formability [8]. In applications where high efficiency is expected, copper is preferred because of its superior electrical conductivity compared to aluminium. There are also studies in which both copper and aluminium are used together to leverage the properties of each material simultaneously. Akçomak and Partal, using a 7.5 kW, 4-pole squirrel-cage induction motor in the IE2 efficiency class as a reference, conducted a study employing both aluminium and copper conductors and reported that the efficiency class was upgraded to IE4 [27].

A review of the literature shows that factors such as the motor's geometric configuration and the combination of stator and rotor slots can offer advantages as well as present disadvantages depending on the selected design. Therefore, manufacturers seek to identify the optimal combination of design parameters to achieve the best motor performance. In a study focusing on the architecture of stator and rotor slots, Babypriya and Gomathi analysed a reference three-phase induction motor using FEM by varying the number of rotor bars (and hence the slots) along with the conductor material [20]. In this study, where the number of stator slots was kept fixed and the effects of rotor slot count and rotor bar material on power, torque, current, speed, efficiency, and power factor were investigated, it was observed that a 19-bar configuration with aluminium conductors provided the best overall performance [20]. In the present paper, to evaluate the overall performance of critical design parameters for electric motors, FEA analyses were conducted on a YASA-type AFIM with 29, 31, 35, 37, and 41 rotor bars using both aluminium and copper conductor materials. This study provides a general comparison opportunity for the YASA-type AFIM, which has been explored only to a limited extent in the literature.

The parameters of the YASA-type AFIM with a double-rotor, single-stator architecture considered as the reference in this study are presented in Table 2. In electric motors, electrical steels are generally accepted as rotor and stator materials due to their magnetic capabilities and core characteristics [28] in this study, JFE_Steel_50JN290, which possesses these properties was used. To evaluate motor performance across dynamic speed applications, the motor was analysed at 1000, 2000, and 3000 rpm. The reference motor has an output power of 6.4 kW, 6 poles, and 9 stator slots.

Table 2. Design parameters of the reference YASA-type AFIM

Parameter	Value	Unit
Power	6.4	kW
Number of poles	6	-
Speed	3000	rpm
Moment	20.37	Nm
Outer diameter	220	mm
Inner diameter	130	mm
Rotor skew	0	deg (°)
Stator thickness	35	mm
Rotor thickness	30	mm
Air gap	0.65	mm
Stator windings	copper	-
Rotor material (Laminated)	JFE_Steel_50JN290	-
Stator material (Laminated)	JFE_Steel_50JN290	-
Rotor conductor material	copper	-

The fractional slot concentrated winding (FSCW) technique is widely used in induction motors due to its advantages, including its capability for flux weakening, positive effects on efficiency, contribution to torque density, increased slot fill factor, and overall enhancement of power density [29]. The YASA-type AFIM designed in this study employs this winding structure. Compared to distributed winding techniques, FSCW offers better fault tolerance [30] and allows the use of a segmented stator architecture with the benefit of a high slot fill factor [31]. However, in designs using the FSCW technique, factors such as air gap, slot-to-pole configuration, slot opening shape, and the number of winding layers must be carefully considered [32,33]. For each pole number, there exists an optimum number of stator slots that provides the maximum fundamental winding factor [52]. In the YASA-type

AFIM designed here, the slot-to-pole combination was determined by taking these effects into account. For the selected 6/9 configuration, the fundamental winding factor $k_{\omega 1}$ is high at 0.866, while the harmonic index h_{shi} is low at 3.0822. Therefore, the chosen winding structure enables efficient magnetic field generation with a high fundamental winding factor while simultaneously minimizing harmonic components, thereby enhancing overall motor performance.

During the design phase of the AFIM, the overall dimensions of the considered motors can be estimated using sizing equations [34,35]. Assuming that the magnetic flux density in the air gap B_δ is sinusoidal, it can be expressed as shown in Equation (1) [34].

$$B_\delta = \hat{B}_\delta \sin\left(\frac{p}{2}\theta - \omega_s t\right) \tag{1}$$

In Equation (1), B_δ represents the amplitude of the magnetic flux density, p denotes the number of poles, θ is the mechanical angle in the air gap region, and ω_s represents the electrical angular frequency.

By integrating Equation (1) over the area of a single pole, the fundamental air-gap flux per pole, ϕ_P, for each air gap can be determined as shown in Equation (2) [34].

$$\phi_P = \frac{(D_o^2 - D_i^2)\hat{B}_\delta}{2p} \tag{2}$$

In this context, D_o represents the outer diameter of the motor, whereas D_i denotes the inner diameter.

Following the determination of the output power, which is considered the most critical parameter for the motor to be designed, the outer diameter can be calculated theoretically based on this parameter. While the sizing equations developed by Woolmer [36] are employed for the AFIM with YASA topology, the nominal power is determined using Equation (3).

$$P = \frac{m}{m_1}\frac{\pi^2}{4} k_e k_i k_p B_g A_s \frac{fe}{p}(1 - k_d^2)\frac{1 + k_d}{2} D_o^3 \tag{3}$$

In this context, m_1 represents the number of stator phases, m denotes the number of phases, k_e stands for the electromotive force factor, and k_i signifies the current wave factor. Furthermore, k_p represents the electrical power waveform factor, B_g is the flux density in the air gap, A_s refers to the electrical loading, fe denotes the electrical frequency, and p indicates the number of pole pairs. While k_d represents the ratio of the motor's internal to external diameter, D_o signifies the outer diameter.

The electrical loading can be determined by means of Equation (4).

$$A_s = \frac{2m_1 N_{ph} I_{rms}}{\pi Do\left((1 + k_d)\,/\,2\right)} \tag{4}$$

In Equation (4), N_{ph} represents the number of turns per phase, while I_{rms} denotes the root-mean-square (RMS) current value. By utilizing Equations (3) and (4), the outer diameter of the motor can be calculated as follows:

$$D_o = \left(\frac{T}{(m/m_1)(\pi/8)kek_ik_pB_gA_s(1-k_d^2)((1+k_d)/2)} \right)^{1/3} \quad (5)$$

Once the outer diameter is obtained, the inner diameter can be calculated by means of Equation (6).

$$k_d = \frac{D_i}{D_o} \quad (6)$$

The maximum magnetic flux in the rotor yoke $\phi_{r,y}$ and the maximum magnetic flux in the rotor teeth, $\phi_{r,t}$ are determined with the aid of Equations (7) and (8), respectively [34].

$$\phi_{r,y} = \frac{\phi_P}{2} \quad (7)$$

$$\phi_{r,t} = \frac{\pi(D_o^2 - D_i^2)\hat{B}_\delta}{4Q_r} \quad (8)$$

In this context, Q_r denotes the number of rotor slots.

From this, the axial length of the rotor yoke $l_{r,y}$is determined using Equation (9) [34].

$$l_{r,y} = \frac{2\phi_{r,y}}{(D_o - D_i)\hat{B}_{r,y}C_{r,lam}} = \frac{\hat{B}_\delta(D_o + D_i)}{2p\hat{B}_{r,y}C_{r,lam}} \quad (9)$$

In Equation (9), $\hat{B}_{r,y}$ represents the magnetic flux density in the rotor yoke, whereas $C_{r,lam}$denotes the rotor lamination stacking factor.

Regarding the stator section, the maximum magnetic flux in the stator teeth $\phi_{s,t}$ is determined by means of Equation (10) [34].

$$\phi_{s,t} = \frac{\pi(D_o^2 - D_i^2)\hat{B}_\delta}{4Q_s} \quad (10)$$

In this context, Q_s denotes the number of stator slots.

The inner stator tooth width, $w_{s,t,inner}$ and the stator slot width, $w_{s,sl}$ are determined as follows [34]:

$$w_{s,t,inner} = \frac{\pi\hat{B}_\delta D_i}{Q_s\hat{B}_{s,t}C_{s,lam}} \quad (11)$$

$$w_{s,sl} = \tau_{s,inner} - w_{s,t,inner} \quad (12)$$

In Equations (11) and (12), $\hat{B}_{s,t}$ represents the maximum flux density in the stator teeth, while $\tau_{s,inner}$ denotes the stator slot pitch at the inner diameter of the motor.

2. Modelling and Analysis Method

Although AFMs require 3D design due to their inherent architectures, 2D modelling approaches are recognized as a viable alternative for designers. In their study, Aslaner and Akar performed a comparative analysis by implementing both 2D and 3D modelling of a YASA-type AFIM, highlighting the advantages of 2D modelling in terms of computational time [37]. However, evaluating AFIMs using a 2D FEM model presents challenges due to the axial nature of the flux [2]. To enable 2D FEA modelling of an AFIM, the motor is assumed to be linear [7]. Given the disk-shaped structure of the AFM, where the stator and rotor are positioned in parallel, a 2D linear model is obtained by 'unrolling' a section taken at the mean diameter [8]. The conversion of a 3D YASA AFIM model into its equivalent 2D model is illustrated in Figure 2.

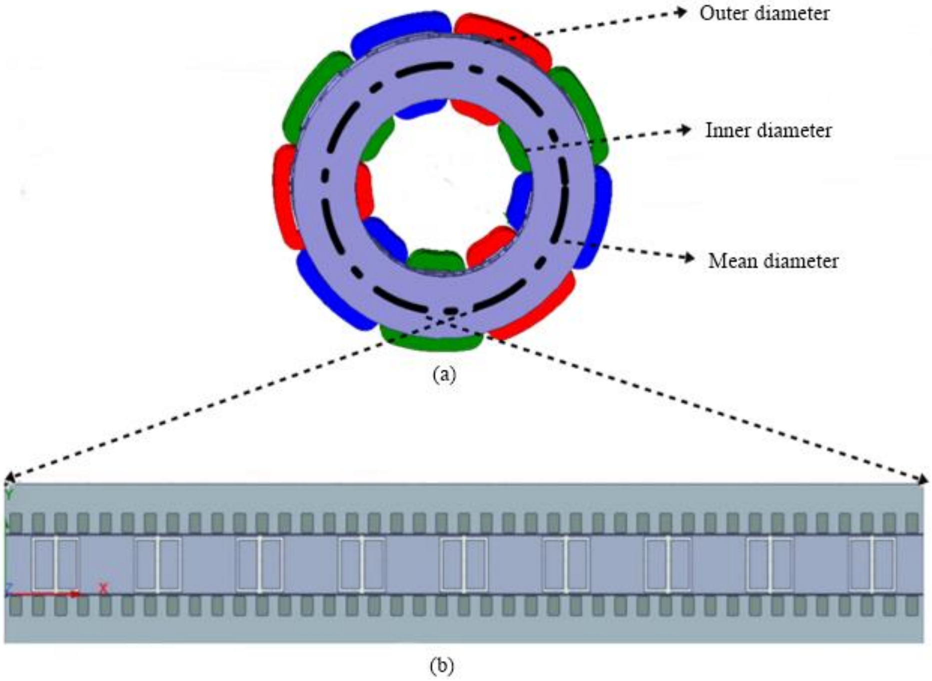

Figure 2. 3D model (a) and 2D model (b) representation of the YASA-type AFIM.

While the rotational motion in the 3D model originates from its axial structure, it functions as a linear translation in the 2D model due to its straightened geometry within the simulation environment. Consequently, whereas the speed parameter is measured in revolutions per minute (rpm) for the 3D model, it is processed as meters per second (m/s) for the 2D model. To derive the 2D model, the area of the circular section taken from the 3D model is denoted as A_C while the rectangular area of the 2D linear model is assumed to be A_r. The values of A_C and A_r are calculated using Equations (13) and (14), respectively [38].

$$A_C = \frac{\pi}{2p}(D_o^2 - D_i^2) \tag{13}$$

$$A_r = \frac{(D_o^2 - D_i^2)}{2} \cdot \frac{\pi(D_0 + D_i)}{p} = \frac{\pi}{2p}(D_0^2 - D_i^2) \tag{14}$$

Since the AFM structure is inherently suited for a 3D modelling approach, certain adverse effects arise from its inability to be fully represented in a 2D model. In particular, end-winding parameters must be addressed separately for the 2D model [39]. When 2D modelling is performed using FEA, the third dimension (z-axis) is defined by the stator active length R_a. The value of R_a is determined via Equation (15).

$$R_a = \frac{D_o - D_i}{2} \quad (15)$$

In modern variable speed drives utilized for electric motors, it is well-recognized that sensitive and continuous speed control, along with permanent stability and high efficiency, has become a necessity. Advancements in static converters have increased the interest in the transient performance of induction motors under adjustable frequency supplies for speed-controlled applications [40]. Induction motor drives fed by Current Source Inverters (CSIs) are known as safe, robust, and highly efficient controllable alternating current drives [41]. In all simulation studies of the dual-rotor single-stator YASA-type AFIM analysed via FEA, the motor was driven by a current source. The three-phase balanced sinusoidal current equations supplied to the stator windings are provided below, respectively.

$$I_k = I_{max} \cdot sin\left(2\pi f t - (k-1)\frac{2\pi}{3}\right) k\epsilon_{\{1,2,3\}} \quad (16)$$

where I_k denotes the instantaneous stator phase currents, with $k\epsilon_{\{1,2,3\}}$ designating phases A, B, and C, respectively. In this unified mathematical representation, I_{max} represents the maximum peak amplitude of the phase current, f signifies the electrical supply frequency, and t indicates the operational simulation time step.

To evaluate the capabilities of induction motors under varying load conditions, they must be simulated under dynamic slip values. In this manner, the overall performance data of the motor can be analysed as a function of slip. While the slip setting determines the operating performance and electromagnetic torque parameters under nominal load conditions, it also dictates the optimum slip value for the maximum efficiency of a squirrel-cage induction motor [42]. In this study, to provide researchers with a comprehensive performance evaluation, analyses were conducted across a wide speed scale within a slip range of 1% to 6%.

To provide researchers with a comprehensive evaluation opportunity for YASA-type AFIMs, which have limited research availability in the literature, the designed motors were evaluated based on average electromagnetic torque, torque ripple, losses, and efficiency; ultimately, the optimum motor architecture was determined using a normalized performance index for the optimization of numerous parameters.

3. Results and Discussion

It is well-established that the slip parameter is critical in evaluating the performance of induction motors. Slip, defined as the ratio of the difference between the synchronous speed n_s of the rotating magnetic field in the stator and the actual rotor speed to the synchronous speed, is close to unity at startup due to the minimum rotor speed. As the rotor speed increases, the slip value approaches zero. When different rotor bar materials are selected, the maximum torque values occur at different slip regions because of the varying electrical conductivity of the conductor bars. For the analytical evaluation of torque and speed characteristics, the torque value can be calculated using Equation (17), derived from the equivalent circuit of a squirrel cage induction motor which directly accounts for the rotor bar resistance and reactance.

$$T = \frac{3V\ th^2\ R_2' \ / \ s}{\omega_{sync}[(R_{th} + R_2 \ / \ s)^2 + (X_{th} + X_2)^2]} \tag{17}$$

In Equation (17), T represents the electromagnetic torque, V_{th} is the Thevenin equivalent voltage, ω_{sync} denotes the synchronous angular speed, R_{th} and X_{th} are the Thevenin equivalent resistance and reactance, respectively. Furthermore, X_2 represents the rotor leakage reactance, s is the slip, and R_2' denotes the rotor resistance referred to the stator.

As observed here, the resistance of the rotor bar material and the slip factor are critical parameters influencing the torque value. Although aluminium is generally preferred as the rotor bar material under market conditions, the increasing interest in high-efficiency motors has led to the growing use of copper. By utilizing copper bar materials, a 54% improvement can be achieved regarding losses associated with the squirrel cage [43]. The torque-slip characteristics obtained from FEA analyses for aluminium and copper materials across five distinct stator-rotor slot/bar configurations (designated via alphanumeric codes in Section 3) are presented in Figure 5. The simulations, conducted via Ansys software, were performed on a workstation equipped with an Intel Core Ultra 7 265K 3.9 GHz processor, 20 cores, and 256 GB of RAM. In the analyses carried out through parametric analyses, the total simulation time was processed as 0.2 s with a time step of 0.21 ms to evaluate motor performance with maximum accuracy, the interval between 0.16 s and 0.2 s was taken as the basis for analysis.

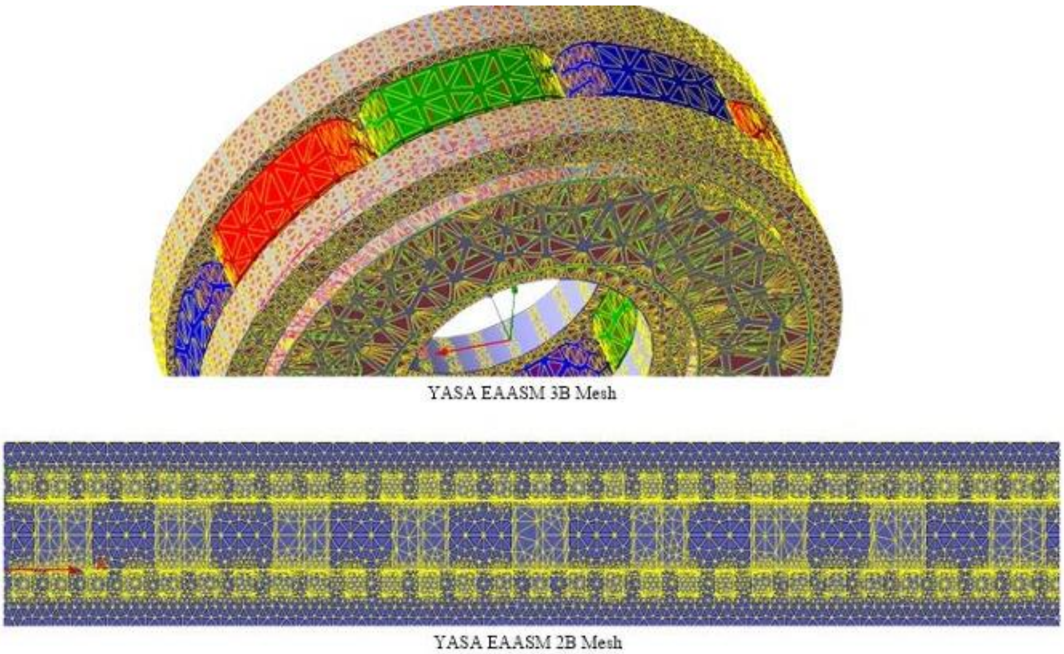

Figure 3. 3D (top) and 2D (bottom) mesh architectures of the YASA-type AFIM [37].

In Figure 3, which presents a comparison between 2D and 3D modelling for the YASA-type AFIM architecture [37], an increase in the mesh density is observed for the 3D model due to the inclusion of the axial dimension; it is well-known that this situation significantly increases the computational cost.

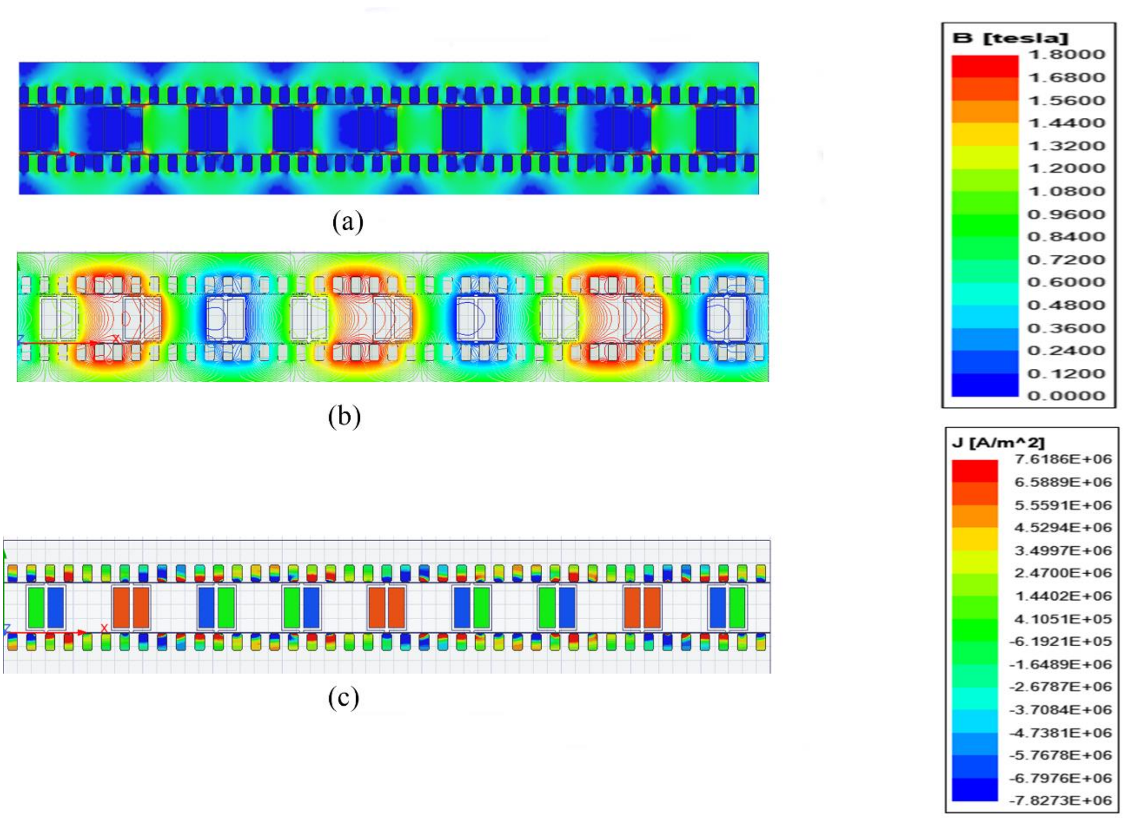

Figure 4. Representation of (a) magnetic flux density, (b) magnetic flux lines, and (c) current density in rotor bars and stator windings of the reference YASA-type AFIM.

Simulation results for the reference motor indicate that the average magnetic flux density is 0.96 T, while the average current density in the stator windings and rotor bars is 3.49 A/mm². Figure 4 illustrates the flux density distribution (a), magnetic flux lines (b), and the induced current density distribution across the stator windings and rotor bars (c) on the 2D linear model.

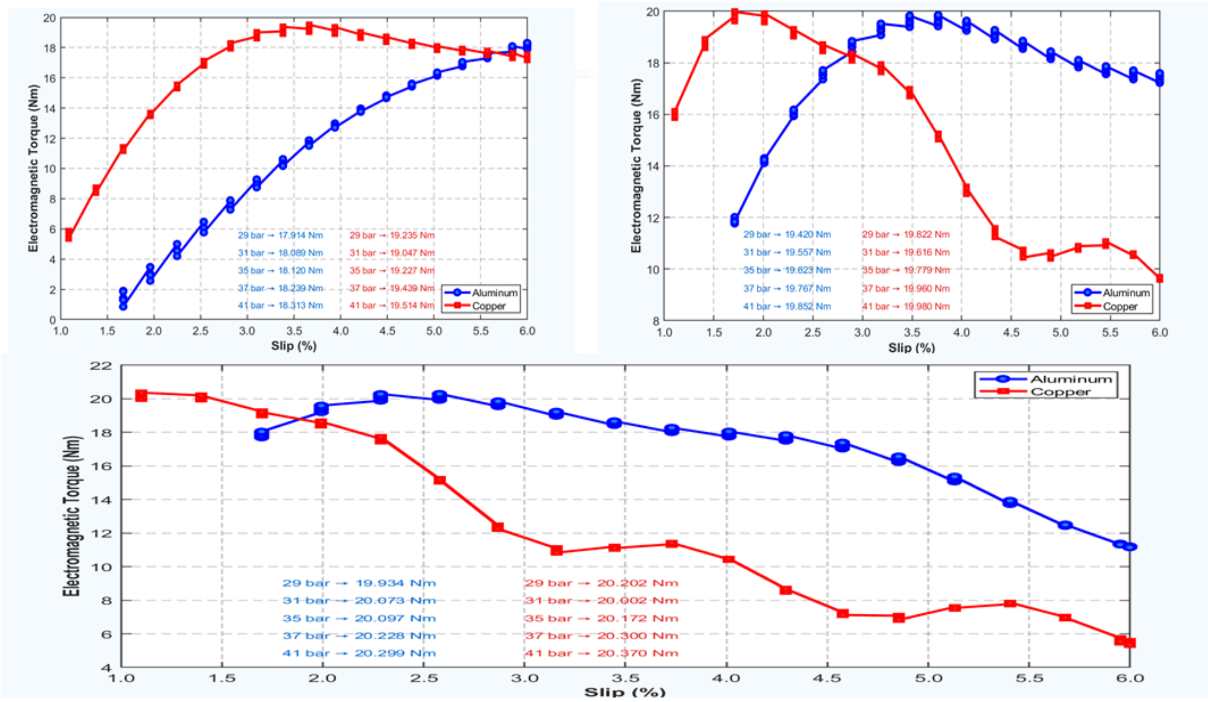

Figure 5. Torque-slip (T-s) characteristics of aluminium and copper rotor bar materials at synchronous speeds of 1000 rpm (top left), 2000 rpm (top right), and 3000 rpm (bottom).

Speed-dependent results were considered as they provide a robust option for assessing motor performance in dynamic speed applications. To investigate the effects of the number of rotor bars on average torque and the impact of material changes on torque characteristics under load, aluminium and copper materials were simulated over a wide speed range for the five designated rotor configurations.

Upon examining the graphs, it is observed that for the aluminium rotor material, the torque value increases with the number of bars across all speed conditions. In the case of copper, which generally yields higher torque values compared to aluminium, the lowest torque data was observed with the 31-bar structure, while the maximum torque was achieved with the 41-bar configuration. When aluminium is selected as the rotor bar material, maximum torque is reached in the high-slip region (6%) at low speeds; however, as the speed parameter increases, the slip region where maximum torque occurs is found to regress. For copper, maximum torque is reached in the nominal slip region (3.5%) at low speeds, and similar to aluminium, this slip region decreases as speed increases. According to the literature, the increase in rotor reactance with higher frequencies reduces the slip value required for maximum torque; furthermore, since the conductivity of aluminium is lower than that of copper, it is expected that the maximum torque slip for aluminium remains higher than for copper across all speed levels.

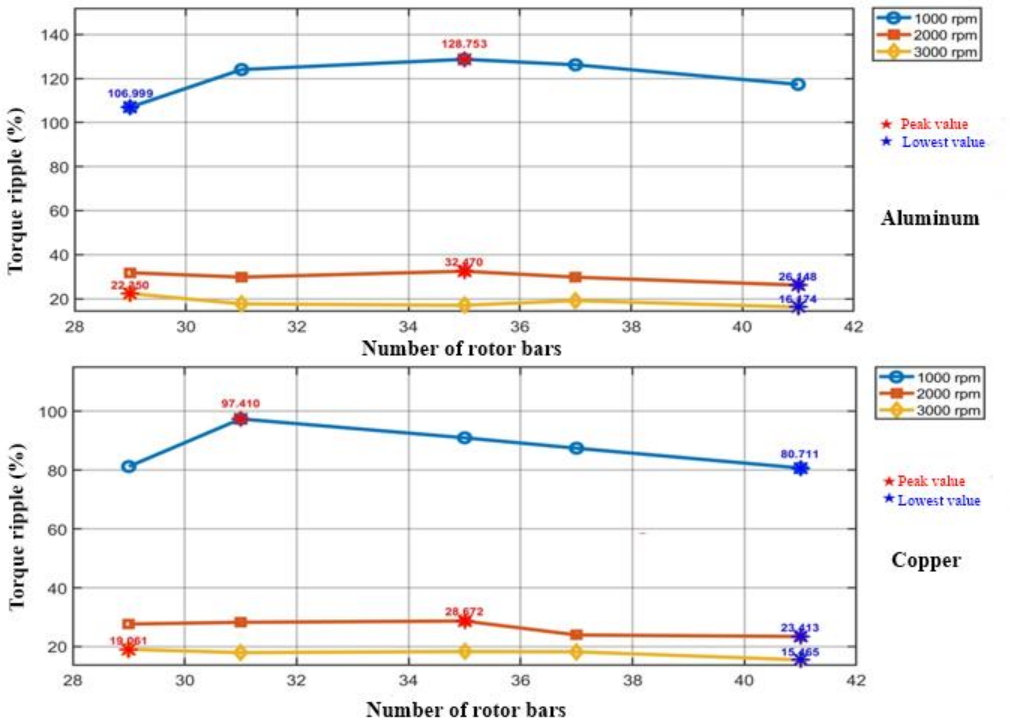

Figure 6. Comparison of torque ripple based on the number of rotor bars for aluminium (top) and copper (bottom) materials.

Upon examining Figure 6, it is observed that for the aluminium rotor bar material, the 9/29 and 9/41 stator-rotor slot/bar combinations exhibit the lowest torque ripple performance across simulations at various speeds, respectively. For the same rotor bar material, the highest torque ripple is observed in the 9/35 and 9/29 combinations.

Regarding copper, it is observed that the lowest torque ripple values across all speeds were obtained with the 9/41 stator-rotor slot structure. Conversely, the highest torque ripple data was identified in the 9/31 and 9/35 stator-rotor slot configurations.

In the literature, copper stands out compared to aluminium not only due to its lower resistance but also for its lower losses and superior thermal capabilities. In addition to advantages such as higher tensile strength, excellent conductivity, and a lower coefficient of thermal expansion, copper is more costly than aluminium [20]. Consequently, despite causing lower conductivity and higher losses, aluminium remains a widely preferred choice due to its cost-effectiveness.

Upon reviewing the literature, it is observed that power losses in AFIM structures are evaluated in five categories [44]. Copper losses, which arise from the Joule heating generated by the current passing through the stator windings and rotor bars, are calculated according to the I^2R law [44]. In this study, since a 2D linear FEA model is preferred for computational efficiency, the precise 3D spatial distribution of electromagnetic losses and localized saturation effects are simplified. To quantify the deviation caused by this 2D approximation, a 3D reference FEA model was verified under identical nominal conditions, building upon the validated 2D/3D quantification methodologies established in [37]. The comparative analysis reveals that due to the restriction of flux paths in the 2D plane and the resulting overestimation of core losses, the 2D model yields higher total power losses compared to the

3D reference (1547 W in 2D versus 1436 W in 3D), presenting a quantitative error margin of approximately 7.73%. This calculated correction factor was analytically integrated into the final efficiency and performance evaluations in Section 4 to ensure high scientific accuracy. Iron losses, resulting from electromagnetically induced eddy current and hysteresis losses in the stator and rotor cores, are calculated for this 2D AFIM model using time-harmonic FEA electromagnetic analysis [38]. Mechanical losses occurring due to friction in the bearings are calculated using Equation (18) [14].

$$Q_{bearing}{=}0.06k_{fb}\left(m_{rotor}+m_{shaft}\right)n \tag{18}$$

Where the equation above, expressed as a function of the bearing quality factor ($Q_{bearing}$) as a function of the bearing friction coefficient k_{fb}, rotor mass m_{rotor}, shaft mass m_{shaft} and the rotational speed (n). Windage (friction) losses, which arise from the wall shear stress at the end-cap region applied to the fan blades on the rotor surface or from the air within the air gap, along with all remaining losses, are characterized as stray load losses; these are estimated to constitute 8% of the total power loss [45]. For the YASA-type AFIM discussed in this article, stray losses have been included in the calculation as a component of the core loss.

The total losses and core losses for the YASA-type AFIM model addressed in this study are given in Equations (19) and (20), respectively; the Bertotti loss model [46] was adopted for the calculation of the core losses.

$$P_{loss}=P_{cu,r}+P_{cu,s}+P_{core} \tag{19}$$

$$P_{core}=P_{hys}+P_{e\,d\,d}+P_{ex} \tag{20}$$

In Equations (19) and (20), $P_{cu,r}$, $P_{cu,s}$, and P_{core} represent the rotor losses, stator losses, and core losses, respectively. The core losses are divided into three components [46], where P_{hys} denotes hysteresis losses, $P_{e\,d\,d}$ denotes eddy current losses, and P_{ex} represents the excess (additional) losses.

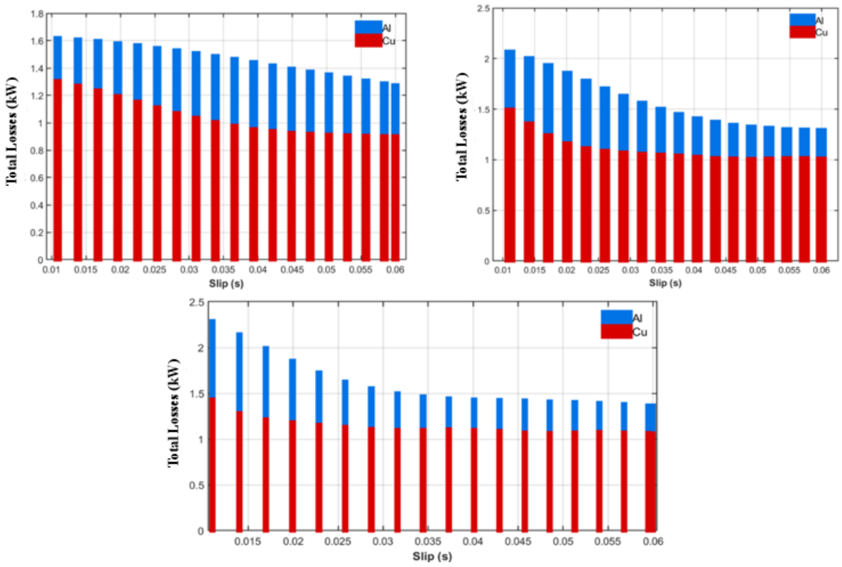

Figure 7. Comparison of total power losses for aluminium and copper rotor bar materials at synchronous speeds of 1000 rpm (top left), 2000 rpm (top right), and 3000 rpm (bottom).

Upon examining the loss data from the simulation results, it was observed that losses increased in direct proportion to the count of bars for both material types. This can be attributed to the increase in eddy current losses resulting from the effect of the slot count on slot leakage reactance [47]. As shown in Figure 7, due to the resistance effect stemming from the intrinsic properties of aluminium and copper, aluminium exhibits higher total losses than copper in all cases, as expected. Regarding total losses, a linear increase is observed for aluminium across all speeds; however, in the case of copper, a tendency for losses to decrease in the high-frequency region was identified. At high frequencies, the current is confined to a thin layer on the conductor due to the skin effect [47]. The general consensus indicates that the current effectively penetrates up to the skin depth δ, which is defined by Equation (21) [47].

$$\delta = \sqrt{\frac{2}{\omega\mu\sigma}} = \frac{1}{\sqrt{\pi f \mu_0 \mu_r \sigma}} \tag{21}$$

As seen in the equation above, where δ is the skin depth, ω is the angular frequency, f is the operating frequency, μ_0 is the permeability of free space, μ_r is the relative permeability and σ is the electrical conductivity; this relationship represents the skin effect mechanism. Thus, the skin effect is expected to remain limited for copper which possesses high conductivity in the high-frequency region, and it is understood that this situation reduces the associated losses. Table 3 provides a general comparison of torque ripple, efficiency, and loss values within the operating region where maximum torque is achieved in the analyses conducted via FEA.

Table 3. Comparison of YASA-type AFIM with different rotor slots and materials in terms of torque, torque ripple, efficiency, and total losses at various speeds.

Rotor bar material/ stator/rotor slot number	Slip (s)	Speed (rpm)	Torque (Nm)	Torque ripple (%)	Efficiency (%)	Total losses (W)
	0.059	1000	17.91	25.89	60.74	1209
Al-9/29	0.037	2000	19.41	19.95	74.23	1408
	0.025	3000	19.93	22.34	79.81	1580
	0.036	1000	19.23	21.47	67.48	969
Cu-9/29	0.020	2000	19.82	20.10	78.12	1160
	0.014	3000	20.20	19.06	83.20	1278
	0.059	1000	18.08	27.40	60.75	1220
Al-9/31	0.037	2000	19.55	18.83	74.26	1416
	0.025	3000	20.07	17.61	79.84	1589
	0.036	1000	19.05	19.48	67.42	962

Cu-9/31	0.017	2000	19.61	22.85	77.08	1217
	0.011	3000	20.00	23.32	81.81	1392
	0.059	1000	18.11	25.85	60.35	1243
Al-9/35	0.037	2000	19.62	19.47	74.11	1433
	0.025	3000	20.09	16.99	79.67	1607
	0.036	1000	19.22	19.70	67.49	968
Cu-9/35	0.017	2000	19.77	21.50	77.08	1229
	0.011	3000	20.17	24.18	81.75	1410
	0.059	1000	18.23	23.58	60.28	1255
Al-9/37	0.037	2000	19.76	18.61	74.16	1440
	0.025	3000	20.22	19.11	79.71	1615
	0.036	1000	19.43	18.21	67.67	971
Cu-9/37	0.017	2000	19.95	22.26	77.15	1234
	0.011	3000	20.30	21.97	81.77	1417
	0.059	1000	18.31	20.88	60.02	1275
Al-9/41	0.037	2000	19.85	16.31	74.10	1451
	0.025	3000	20.30	16.17	79.66	1626
	0.036	1000	19.51	16.85	67.64	976
Cu-9/41	0.017	2000	19.98	18.49	77.08	1241
	0.011	3000	20.37	20.28	81.68	1431

When the results are evaluated, it is observed that the torque value increases with the rotor bar count for both rotor bar materials. This situation is attributed to the increase in the quantity of parallel paths through which the current is distributed in the rotor cage as the bar count expands, leading to a reduction in the rotor equivalent resistance and a subsequent increase in rotor current, which elevates the electromagnetic torque. For both aluminium and copper, efficiency tends to increase across all bar counts as speed increases. This behaviour, expected in induction motor structures, is caused by the increase in mechanical output power at higher speeds, while losses remain relatively low compared to the input power. It is observed that selecting aluminium as the rotor bar material results in higher rotor resistance compared to copper, leading to higher rotor losses that become more pronounced as speed increases. Finally, regarding torque ripple, it is observed that ripple tends to decrease with speed when aluminium is used, whereas the opposite is true for copper. This can be attributed to the high rotor resistance of aluminium, which helps dampen harmonic currents and weaken slot harmonics at higher speeds, thereby reducing ripple. In the case of copper, it was found that increasing speed leads to higher ripple in all configurations except for the 9/29 geometry. This phenomenon indicates that the low resistance of copper makes slot harmonics more prominent, intensifying the rotor-stator interaction and consequently increasing torque ripple. The absence of this trend in the 9/29 geometry for copper suggests that slot harmonics are at a minimum in this specific structure due to the bar count.

Comparative Performance Evaluation

Considering the limited resources available in the literature for the designed YASA-type AFIM structure, a comprehensive analysis was conducted encompassing various rotor bar materials, different rotor bar counts, and a wide speed range. To facilitate the selection of the optimum rotor bar count and material using the obtained data, a NPI was employed. The metric for the NPI was derived using Equation (22).

$$PI = \frac{T_{avg} * \eta}{R_{ipple} * L_{oss}} \tag{22}$$

In Equation (22), T_{avg} represents the average torque, η denotes the efficiency, R_{ipple} signifies the torque ripple, and L_{oss} expresses the total losses.

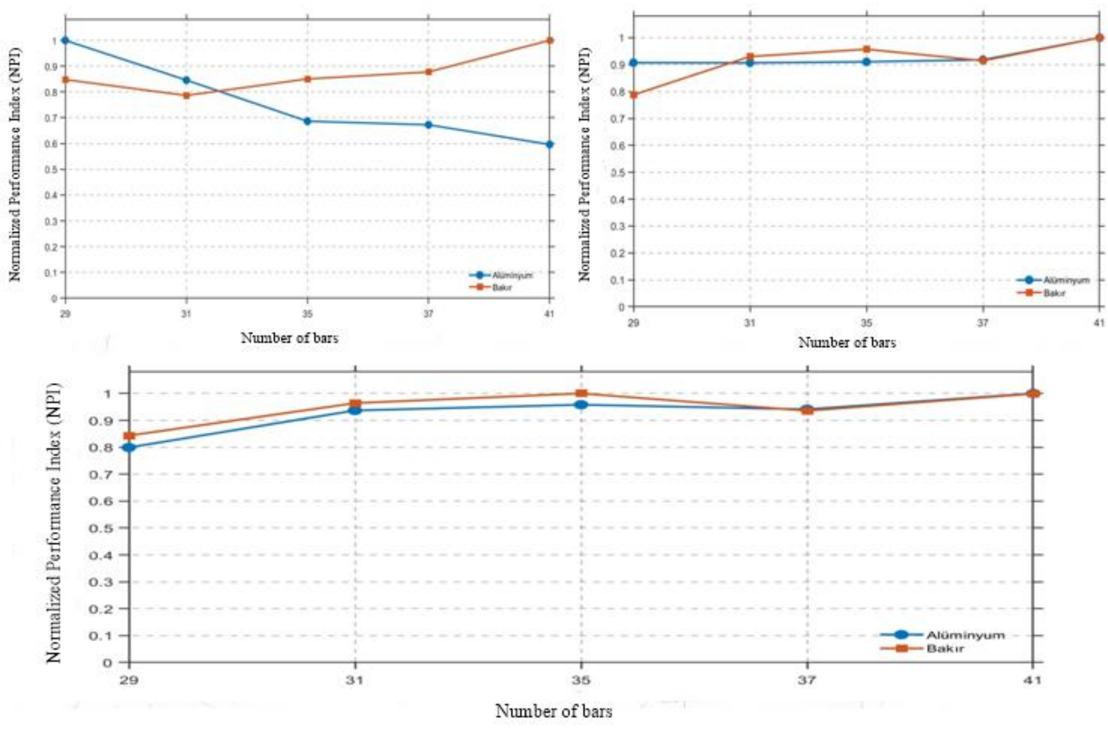

Figure 8. Performance comparison based on the NPI for different rotor bar materials and slot combinations at 1000 rpm (top left), 2000 rpm (top right), and 3000 rpm (bottom).

Upon examining Figure 8, it is observed that for the YASA-type AFIM architecture, the optimum stator-rotor slot geometry is 9/41 across the entire operating speed range when copper is used as the rotor material. In the case where aluminium is selected as the rotor material, the optimum stator-rotor slot geometry is found to be 9/29 at an operating speed of 1000 rpm, whereas it converges to 9/41 at speeds of 2000 and 3000 rpm.

4. Conclusions

This article investigates the overall performance of a YASA-type AFIM structure across a wide speed range by varying the rotor bar count and material. The effects of these parameters on torque, torque ripple, efficiency, and losses were examined, and the motor architecture was simulated under various conditions to determine the optimum configuration. Without altering the stator, rotor bar counts of 29, 31, 35, 37, and 41 were selected, and analyses were conducted for both aluminium and copper materials at speeds of 1000, 2000, and 3000 rpm. To evaluate multiple parameters effectively, a NPI was utilized, identifying the 9/41 stator-slot / rotor-bar combination with copper rotor material as the optimum architecture, which delivers a peak torque of 20.37 Nm and an efficiency of 81.68% at 3000 rpm.

When aluminium was preferred, the 9/29 slot/bar combination stood out at 1000 rpm by restricting the torque ripple to 25.89% compared to the 27.40% observed in the 9/31 design, while the 9/41 combination became prominent at 2000 and 3000 rpm by minimizing the torque ripple to its lowest value of 16.17%. The results reflect the characteristic differences between copper and aluminium; although copper, with its higher conductivity, generally exhibits a 5.1% to 7.3% superior torque density, it was observed to lag behind in certain operating conditions. Specifically, at 3000 rpm within the 9/41 configuration, the copper rotor yields a higher torque ripple of 20.28% compared to the aluminium rotor's 16.17%, demonstrating that higher material conductivity can escalate ripple characteristics at elevated frequencies.Furthermore, since the designed motor was analysed using a 2D transient FEA model, a comparison was made with a 3D reference model under identical nominal conditions. The comparative analysis reveals that due to the restriction of flux paths in the 2D plane, the 2D model overestimates the total power losses by a quantitative error margin of approximately 7.73% (1547 W in 2D versus 1436 W in 3D), validating the necessity of 3D modelling for exact loss profiling in AFIM architectures.

This study, which investigates the YASA topology commonly researched for AFPM architectures in the literature within the context of AFIM structures, aims to provide a comprehensive evaluation for researchers and contribute to this field, where research opportunities remain relatively limited. The design presented in this article offers an opportunity for experimental validation in future studies. Furthermore, while thermal performance analyses are required for various speed operations, different stator-rotor slot geometries must be investigated to minimize losses while increasing torque density. With the advancement of computational capabilities in modern technology and the development of optimization materials in this field, it is evident that the proposed design can be further improved. Given the scarcity of comprehensive studies on this topology in the literature, this structure demands further investigation.

Ethics in Publishing

There are no ethical issues regarding the publication of this study

Author Contributions

All authors have contributed equally to this work.

References

[1] De Almeida, A. T., Ferreira, F. J., & Baoming, G. (2013, April). Beyond induction motors—Technology trends to move up efficiency. In *49th IEEE/IAS Industrial & Commercial Power Systems Technical Conference* (pp. 1-13). IEEE.

[2] Kahourzade, S., Mahmoudi, A., Ravji, R., & Soong, W. L. (2019, September). Line-Start axial-flux PM motors: Introduction of a new machine topology. In *2019 IEEE energy conversion congress and exposition (ECCE)* (pp. 7027-7034). IEEE.

[3] Amin, S., Khan, S., & Bukhari, S. S. H. (2019, January). A comprehensive review on axial flux machines and its applications. In *2019 2nd International Conference on Computing, Mathematics and Engineering Technologies (iCoMET)* (pp. 1-7). IEEE.

[4] Mushid, F. C., & Dorrell, D. G. (2017, April). Review of axial flux induction motor for automotive applications. In *2017 IEEE Workshop on Electrical Machines Design, Control and Diagnosis (WEMDCD)* (pp. 146-151). IEEE.

[5] Spooner, E., & Chalmers, B. J. (1988, September). Toroidally-wound, slotless, axial-flux, permanent-magnet, brushless-DC motors. In *Proc. International Conference on Electrical Machines* (Vol. 3, pp. 81-86).

[6] Al-Badi, A., Gastli, A., Bourdoucen, H., & Jervase, J. (2000). Evolution of axial-field electrical machines. *Sultan Qaboos University Journal for Science*, *5*(2), 227-245.

[7] Cao, Z., Mahmoudi, A., Kahourzade, S., Soong, W. L., & Summers, J. R. (2020, December). A comparative study of axial-flux versus radial-flux induction machines. In *2020 IEEE International Conference on Power Electronics, Drives and Energy Systems (PEDES)* (pp. 1-6). IEEE.

[8] Özsoy, M., Kaplan, O., & Akar, M. (2024). FEM-based analysis of rotor cage material and slot geometry on double air gap axial flux induction motors. *Ain Shams Engineering Journal*, *15*(2), 102393.

[9] Dianati, B., Kahourzade, S., & Mahmoudi, A. (2020). Optimization of axial-flux induction motors for the application of electric vehicles considering driving cycles. *IEEE Transactions on Energy Conversion*, *35*(3), 1522-1533.

[10] Nobahari, A., Darabi, A., & Hassannia, A. (2017, February). Axial flux induction motor, design and evaluation of steady state modelling using equivalent circuit. In *2017 8th Power Electronics, Drive Systems & Technologies Conference (PEDSTC)* (pp. 353-358). IEEE.

[11] Cao, Z., Mahmoudi, A., Kahourzade, S., & Soong, W. L. (2021, September). An overview of axial-flux induction machine. In *2021 31st Australasian Universities Power Engineering Conference (AUPEC)* (pp. 1-6). IEEE.

[12] Nasiri-Gheidari, Z., & Lesani, H. (2012). A survey on axial flux induction motors. *Przegląd Elektrotechniczny*, *88*, 300-305.

[13] Mirzaei, M., Mirsalim, M., & Abdollahi, S. E. (2007). Analytical modelling of axial air gap solid rotor induction machines using a quasi-three-dimensional method. *IEEE Transactions on Magnetics*, *43*(7), 3237-3242.

[14] Gieras, J. F., Wang, R. J., & Kamper, M. J. (2008). *Axial flux permanent magnet brushless machines*. Dordrecht: Springer Netherlands.

[15] Du-Bar, C. (2011). Design of an axial flux machine for an in-wheel motor application. *Chalmers Reproservice, Göteborg*, 1-2.

[16] Woolmer, T. J., & McCulloch, M. D. (2007, May). Analysis of the Yokeless and segmented armature machine. In *2007 IEEE International Electric Machines & Drives Conference* (Vol. 1, pp. 704-708). IEEE.

[17] Chang, J., Fan, Y., Zhu, B., Luo, L., Wu, J., Pan, Y., & Kang, P. (2020). Design of a new type Yokeless and segmented armature axial flux machine. *International Journal of Applied Electromagnetics and Mechanics*, *62*(4), 823-834.

[18] Taran, N., Klink, D., Heins, G., Rallabandi, V., Patterson, D., & Ionel, D. M. (2021). A comparative study of Yokeless and segmented armature versus single sided axial flux PM machine topologies for electric traction. *IEEE Transactions on Industry Applications*, *58*(1), 325-335.

[19] Daut, I., Anayet, K., Gomesh, N., Asri, M., & Irwan, Y. M. (2009, December). Comparison of Copper Rotor Bars with Aluminium Rotor Bars Using FEM Software--A Performance Evaluation. In *2009 Second International Conference on Computer and Electrical Engineering* (Vol. 1, pp. 456-459). IEEE.

[20] Babypriya, B., & Gomathi, S. (2021). Numerical analysis on impact of choice of number of rotor slots on performance of three phase induction motor. *Materials Today: Proceedings*, *45*, 2364-2370.

[21] Gyftakis, K. N., & Kappatou, J. (2013). The impact of the rotor slot number on the behaviour of the induction motor. *Advances in Power Electronics*, *2013*(1), 837010.

[22] Lordoglu, A., Gulbahce, M. O., & Kocabas, D. A. (2021). A comprehensive disturbing effect analysis of multi-sectional rotor slot geometry for induction machines in electrical vehicles. *IEEE Access*, *9*, 49590-49600.

[23] Mushid, F. C., & Dorrell, D. G. (2017, April). Review of axial flux induction motor for automotive applications. In 2017 IEEE Workshop on Electrical Machines Design, Control and Diagnosis (WEMDCD) (pp. 146-151). IEEE

[24] Evans, P. D., Brown, D., & Eastham, J. F. (1987, August). A study of permanent magnet disc motor design. In BICEM Proceedings (pp. 729-732).

[25] Spooner, E., & Chalmers, B. J. (1992, November). 'TORUS': A slotless, toroidal-stator, permanent-magnet generator. In IEE Proceedings B (Electric Power Applications) (Vol. 139, No. 6, pp. 497-506). IEE

[26] Finley, W. R., & Hodowanec, M. M. (2002). Selection of copper versus aluminium rotors for induction motors. *IEEE Transactions on Industry Applications*, *37*(6), 1563-1573.

[27] Akçomak, M., & Partal, S. Z. Çift Kafesli Rotorda Alüminyum ve Bakırın Birlikte Kullanımının Asenkron Motor Verimine Etkisinin İncelenmesi. *EMO Bilimsel Dergi*, *12*(2), 15-25.

[28] Momin, A. (2024). Review of Electrical Steels with their Properties and Recent Trends for Improvement. Technology, 17(41), 4270-4286.

[29] Gundogdu, T., Komurgoz, G., & Mantar, B. (2014, April). Implementation of fractional slot concentrated windings to induction machines. In 7th IET International Conference on Power Electronics, Machines and Drives (PEMD 2014) (pp. 1-6). IET.

[30] Cros, J., & Viarouge, P. (2002). Synthesis of high performance PM motors with concentrated windings. IEEE transactions on energy conversion, 17(2), 248-253.

[31] El-Refaie, A. M., & Jahns, T. M. (2004, October). Optimal flux weakening in surface PM machines using concentrated windings. In Conference Record of the 2004 IEEE Industry Applications Conference, 2004. 39th IAS Annual Meeting. (Vol. 2, pp. 1038-1047). IEEE.

[32] Zhu, Z. Q., & Howe, D. (1997, May). Winding inductances of brushless machines with surface-mounted magnets. In 1997 IEEE International electric machines and drives conference record (pp. WB2-2). IEEE.

[33] Reddy, P. B., Jahns, T. M., & El-Refaie, A. M. (2008, October). Impact of winding layer number and slot/pole combination on AC armature losses of synchronous surface PM machines designed for wide constant-power speed range operation. In 2008 IEEE Industry Applications Society Annual Meeting (pp. 1-8). IEEE.

[34] Bitsi, K., Beniakar, M. E., Wallmark, O., & Bosga, S. G. (2020, August). Preliminary electromagnetic sizing of axial-flux induction machines. In *2020 International Conference on Electrical Machines (ICEM)* (Vol. 1, pp. 284-290). IEEE.

[35] Keskin Arabul, F., Senol, I., & Oner, Y. (2020). Performance analysis of axial-flux induction motor with skewed rotor. *Energies*, *13*(19), 4991.

[36] Woolmer, T. J. T. (2009). The Yokeless and segmented armature machine developed for the LIFECar (Doctoral dissertation, University of Oxford).

[37] Aslaner, H., & Akar, M. "Boyunduruksuz ve Segmentli Armatür tipi Eksenel Akılı Asenkron Motorun 2 Boyutlu ve 3 Boyutlu Sonlu Eleman Modelleme Sonuçlarının Karşılaştırılması," in *Proc. 6th International Conference on Recent Academic Studies (ICRAS)*, pp. 5–18, 2026.

[38] Colombo, L. (2021). Electromagnetic sizing of axial-flux induction machines and experimental validation.

[39] Yan, B., Li, X., Sun, Y., & Tan, Y. (2023). End Effect Equivalence in the 2-D Finite Element Analysis of a Line-Start Permanent Magnet Synchronous Motor with Hybrid Solid Rotor. Energies, 16(19), 6766

[40] Lipo, T. A. (1988). Recent progress in the development in solid-state AC motor drives. *IEEE Transactions on Power Electronics*, *3*(2), 105-117.

[41] Bose, B. K. (2005). Adjustable speed ac drives—A technology status review. *Proceedings of the IEEE*, *70*(2), 116-135.

[42] Syed, Q. A. S., Laghari, I. A., Ali, A., Samo, K. A., & Soomro, Z. (2025). Steady state electromagnetic analysis of the squirrel cage induction motor. *Spectrum of Engineering Sciences*, 1353-1360.

[43] Kirtley, J. L., Cowie, J. G., Brush, E. F., Peters, D. T., & Kimmich, R. (2007, June). Improving induction motor efficiency with die-cast copper rotor cages. In *2007 IEEE Power Engineering Society General Meeting* (pp. 1-6). IEEE.

[44] Zhao, A., Chen, H., Boßer, C., & Leksell, M. (2024). FEM and CFD thermal modelling of an axial-flux induction machine with experimental validation. *Case Studies in Thermal Engineering*, *53*, 103879.

[45] Valtonen, M. (2007). *Performance characteristics of an axial-flux solid-rotor-core induction motor*. Lappeenranta University of Technology.

[46] Bertotti, G. (1988). General properties of power losses in soft ferromagnetic materials. *IEEE Transactions on magnetics*, *24*(1), 621-630.

[47] Duan, Y., Zhao, J., Xiong, Y., Wang, H., & Tian, J. (2025). Study on Eddy Current Loss Characteristics and Multi-Objective Optimization of High-Speed Solid Rotor Induction Motors. *Electronics*, *14*(20), 4085.

[48] Özsoy, M., Kaplan, O., & Akar, M. (2023). Implementation of Different 2D Finite Element Modelling Approaches in Axial Flux Induction Motors. *Electric Power Components and Systems*, *51*(19), 2385-2396.

[49] Wang, Q., Wang, J., & Geng, W. (2024, November). Equivalent two-dimensional finite element analysis of axial flux induction motor with double stator and single rotor. In *2024 27th International Conference on Electrical Machines and Systems (ICEMS)* (pp. 2556-2562). IEEE.

[50] Gerçekcioğlu, H. S., & Akar, M. (2021). Efficiency and performance comparison between synchronous reluctance and induction motor in axial flux concept. *Gazi Üniversitesi Fen Bilimleri Dergisi Part C: Tasarım ve Teknoloji*, *9*(2), 297-316.

[51] Montero, M. A. T., Garces, A. E. H., Ladino, J. A. T., & Collao, R. R. W. (2017). Simulation and analysis of an axial flux induction machine. *IEEE Latin America Transactions*, *15*(7), 1263-1269.

[52] Gundogdu, T. (2018). *Advanced non-overlapping winding induction machines for electrical vehicle applications* (Doctoral dissertation, University of Sheffield).

[53] Huang, P., Li, H., & Yang, C. (2021, February). A Yokeless axial flux induction motor for electric vehicles based on grain-oriented silicon steel. In *Journal of Physics: Conference Series* (Vol. 1815, No. 1, p. 012042). IOP Publishing.